INORGANIC CHEMISTRY FRONTIERS

RESEARCH ARTICLE

View Article Online
View Journal | View Issue

Cite this: *Inorg. Chem. Front.*, 2023, **10**, 5144

Recognition, detection and host–guest chemistry of hydrogen peroxide in a fluorescent metal–organic framework with chiral helical channels†

Hong Cai, *[a] Jie-Wen Wu,[a] Xiao-Jun Cai,[a] Zhou Lu, [b] Ya-Liang Lai,[c] Jing-Xuan Sun,[d] Zhuo-Li Yuan,[a] Yang-Ying Huang,[a] Jing-Wen Cai,[a] Wen Lu,[a] Yi-Hong Lu,[a] Hui-Ying Zhang[a] and Dan Li *[c]

Received 11th June 2023,
Accepted 12th July 2023

DOI: 10.1039/d3qi01092a

rsc.li/frontiers-inorganic

Combining supramolecular chemistry and bioscience, metal–organic frameworks (MOFs) built with biomolecules as ligands possess highly ordered structures and unique pores with accessible metal binding sites and rich interactions to drive molecular recognition processes. In this work, a novel purine-based MOF with chiral helical channels has been successfully constructed, named **HSTC-1**, which identifies H_2O_2 with a fluorescence quenching effect. Notably, the successful encapsulation of H_2O_2 could be observed by single-crystal X-ray diffraction. Metadynamics and density functional theory calculations reveal that the adsorption of H_2O_2 molecules through the chiral channels induces chiral distribution of subsequent guests to form a host–guest recognition system of H_2O_2@**HSTC-1**, which slows down the oxidation of the host framework. This work provides unique insights for the construction of intelligent protection matrix materials and is of great significance in the fields of pharmacochemistry and biomedicine.

Introduction

Hydrogen peroxide (H_2O_2) is the most symbolic reactive oxygen species and plays an important physiological role in medicine and the human body.[1,2] However, H_2O_2 is referred to as a 'Jekyll and Hyde' molecule in the scientific literature.[3] Excessive amounts of H_2O_2 in the body will attack cells or biomolecules, including protein structures, liposomes, and DNA, leading to oxidative stress and toxic and lethal chain reactions, and is even associated with severe diseases.[4,5] But a major issue for the application of H_2O_2 probes in biological cells is the lack of reaction retention due to the highly oxidizing nature of H_2O_2, which triggers a reaction once it comes into contact with reactants. The time from the addition of H_2O_2 to the actual experiment usually spans hours, resulting in a constantly changing "background" signal, and it is difficult to guarantee and demonstrate uniform probe distribution in samples, which is also one of the reasons why the identification and quantitative detection of H_2O_2 in cells remains challenging.[6–8]

Metal–organic frameworks (MOFs) have been emerging as one of the most promising materials due to their tunable pore sizes, diverse structures, and exposed metal sites,[9–12] which capture molecules by means of solid–liquid phases without changing their activity and functional groups, providing advantageous conditions for studying their interactions at the atomic level in host–guest chemistry. The utilization of biomolecular linkers[13–17] can enhance the recognition capability of MOFs, and the diversity in the size and shape of channels within MOFs endows them with unique properties.[18–23] Typical examples are adenine-based ZnBTCA, which adaptively recognizes thymidine using sinusoid-like channels to achieve A–T base pairing,[18] and a hierarchical pore Zn-MOF based on 6-benzylaminopurine, which exclusively recognizes acetone through multiple hydrogen bond interactions between hosts and guests.[23]

Purine, an alkaloid in the body, can produce a variety of tautomeric forms influenced by electron transfer.[24] Its rigid

[a]*School of Chemistry and Environmental Engineering, Hanshan Normal University, Chaozhou 521041, P. R. China. E-mail: tiddychen@163.com*
[b]*Department of Chemistry, University of Rochester, Rochester, New York 14627, USA*
[c]*College of Chemistry and Materials Science, Guangdong Provincial Key Laboratory of Functional Supramolecular Coordination Materials and Applications, Jinan University, Guangzhou 510632, P. R. China. E-mail: danli@jnu.edu.cn*
[d]*College of Chemistry & Chemical Engineering, Shantou University, Shantou 515063, P. R. China*

†Electronic supplementary information (ESI) available. CCDC 2225754 (for **HSTC-1**), 2225755 (for H_2O_2@**HSTC-1**), 2225756 (for oxidized-**HSTC-2**), 2225757 (for **HSTC-1a**) and 2225759 (for **HSTC-2**). For ESI and crystallographic data in CIF or other electronic format see DOI: https://doi.org/10.1039/d3qi01092a

structure facilitates the formation of robust MOFs, with the four N atoms of purines having more coordination modes and supramolecular interactions, such as hydrogen bonding. The unique non-covalent interactions between metal ions and purine make their MOFs highly dynamic[25] and provide a prerequisite for the formation of special shaped channels. Herein, a novel three-dimensional chiral MOF, named **HSTC-1**, was successfully constructed using the purine biomolecule. Under mild conditions, **HSTC-1** could capture and identify H_2O_2 using chiral helical channels and successfully decelerate oxidation by strong oxidants. This provides alternative technical support for the identification and detection of H_2O_2.

Results and discussion

Single-crystal X-ray diffraction (SCXRD) analyses revealed that **HSTC-1** crystallizes in an orthorhombic crystal system with a chiral space group of $P2_12_12_1$ (Table S1†). The asymmetric unit contains one crystallographically independent Zn center with tetrahedral coordination geometry. Zn^{2+} binds to N of three different purine ligands and an acetate oxygen atom, forming a mononuclear Zn(purine)$_3$(acetate) secondary building unit (SBU). The polymer chain consists of Zn^{2+} and purine arranged along the 2_1 screw axis in the form of a helix. These 1D helical chains are further connected at the Zn^{2+} centers, giving rise to a three-dimensional framework with one-dimensional helical chiral channels (Fig. 1a–c). It contains an irregular rectangular channel (*ca.* 6.52 Å × 7.56 Å) running along the [100] direction with a porosity of 27.2% per unit cell volume calculated after the removal of the guest molecule acetonitrile. The sinusoid-like chiral helical pores along the *b*-axis connect with the *a*-axis channel (Fig. 1d), while uncoordinated oxycarboxylate oriented toward the channel provides a potential active site for molecular recognition. The spiral chirality of the framework was further determined by means of solid-state circular dichroism (CD) measurements. Bulk samples tend to be uniform mixtures of crystals with opposing chirality, and thus have no Cotton-effect signals, whereas individual crystals with homochirality can be formed by spontaneous resolution. CD spectra exhibit positive and negative Cotton effects at the same positions, confirming that they are enantiotropic (Fig. S10†). A topological description of **HSTC-1** can be achieved by denoting the SBU as a three-connected (3-c) node and purine as a (3-c) node, respectively. Then, it is simplified as a uninodal 3-c net with the point symbol $\{10^3\}$, which has been registered as an *srs* topological type in the Topos Topological Database (TTD) collection (Fig. S8 and topological analysis in the ESI†).

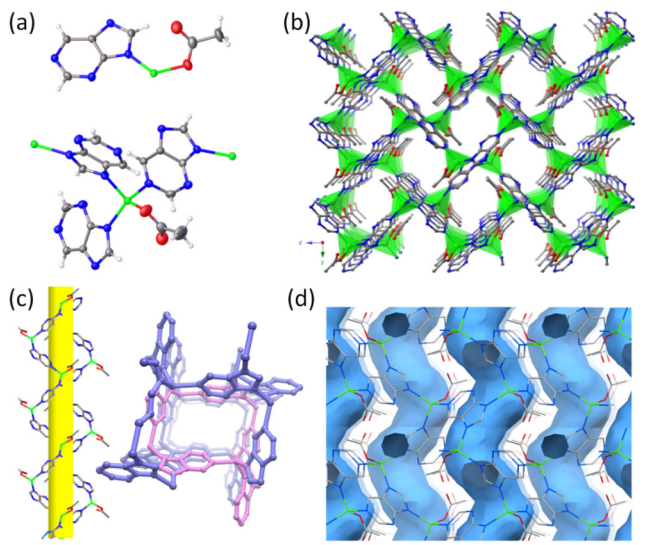

Fig. 1 (a) The asymmetric unit and the coordination environment of **HSTC-1**. (b) The 3D structure with 1D channels viewed along the *a*-axis. (c) Representation of the 2_1 screw axis along the *a*-axis of **HSTC-1**, shown as a yellow cylinder, and the perspective view of the 1D helical chiral channel shown in two different colours, magenta and blue. (d) The chiral helical pores along the *b*-axis are connected with the *a*-axis pore with the contact surface, probe radius: 1.2 Å. Colour codes: C, grey; N, blue; O, red; Zn, green (tetrahedra); H, white or omitted.

N_2 (77 K) and CO_2 (273 K) adsorption experiments were performed on **HSTC-1** to assess its permanent porosity. **HSTC-1** shows normal adsorption capacity and the mode pore-size is 6.86 Å; this accounted for the dominant distribution, which is consistent with the pore size predicted by the single-crystal structure (Fig. S1†). After soaking the synthesized samples in different organic solvents for 24 h, their powder X-ray diffraction (PXRD) patterns still match well with the simulated PXRD patterns from single-crystal data indicating their structural integrity and good chemical stability (Fig. S2a†). Thermogravimetric analysis (TGA) of **HSTC-1** shows that the weight loss of 15.3% below 300 °C is due to the loss of acetonitrile guest molecules, while the host framework starts to collapse above 500 °C, manifesting the excellent thermostability of **HSTC-1** (Fig. S3a†).

Solid **HSTC-1** emitted blue light under ultraviolet light irradiation at room temperature. The broad emission band of **HSTC-1** is located at around 455 nm (λ_{max} = 380 nm) (Fig. S5†). Interestingly, after the addition of 20 μL of 30% H_2O_2, the luminescence of **HSTC-1** showed a quenching effect, which prompted us to explore this phenomenon further (Fig. 2a, S6†). To quantitatively describe the fluorescence signal response of **HSTC-1** to H_2O_2, concentration-dependent fluorescence titration experiments were performed. As shown in Fig. 2a, the fluorescence intensity of the **HSTC-1** acetonitrile suspension decreased distinctively with the addition of H_2O_2. Meanwhile, a linear function correlation between the emission intensity of **HSTC-1** and H_2O_2 concentration was observed, with the Stern–Volmer equation $I_0/I = 0.9983 + 0.0065[M]$ (R^2 = 0.9718) in the range of 0–80 μM (I_0 = luminescence intensity of pristine **HSTC-1**, I = luminescence intensity of **HSTC-1** after the addition of H_2O_2, and [M] is the molar concentration of H_2O_2) (Fig. S7†). Therefore, the sensitivity value could reach 6540 L mol^{-1}, which is comparable to those values of previously reported[2,7,8] materials with moderate sensitivity properties. By calculation using the $3\sigma/k$ formula (σ is the standard deviation of 5 replicating luminescence measurements of blank solutions, and k is the slope of the calibration curve),

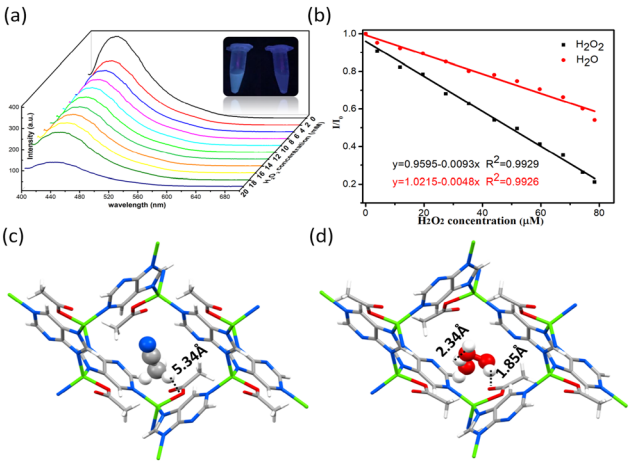

Fig. 2 (a) Emission spectra of **HSTC-1** as a suspension in acetonitrile excited at 380 nm upon the incremental addition of H_2O_2. The inset is a photograph of vials under 365 nm UV light. (b) Corresponding I/I_0 plot after the addition of H_2O_2 and H_2O in the range of 0–80 μM. (c) Pore structures of CH_3CN@**HSTC-1** and (d) H_2O_2@**HSTC-1**. Colour codes: C, grey; N, blue; O, red; Zn, green; H, white.

the detection limit for H_2O_2 was found to be 10.05 ppm. Water is also well-known as a strong fluorescence quencher. Therefore, we compared the fluorescence titration experiment with H_2O under the same conditions and obtained the equation as $I/I_0 = 1.0215–0.0048x$ ($R^2 = 0.9926$). From Fig. 2b, it can be found that the decrease of fluorescence intensity (I/I_0) on dropping H_2O is smaller than that on dropping H_2O_2, indicating that H_2O_2 plays a role in fluorescence quenching with the synergistic effect of H_2O. The absorption spectra of **HSTC-1** acetonitrile solution feature two absorption peaks at 215 nm and 280 nm. Upon H_2O and H_2O_2 being added into the solution, absorbance increases and blue shifts occur at 280 nm. With the addition of H_2O_2, the increase of the relative absorbance ratio of the two peaks (A_{215}/A_{280}) is higher than that with the addition of H_2O (Fig. S11†). Thus, competitive absorption of excitation light by H_2O_2 may reduce the luminescence intensity of **HSTC-1**.[26]

To further clarify the luminescence quenching mechanism, the samples were soaked in 3% H_2O_2 for 2 h and then filtered out for PXRD measurements. No obvious difference in the PXRD pattern was observed compared with the simulated one (Fig. S2c†). Interestingly, it can be seen from Fig. S2c† that the positions of the PXRD peaks of **HSTC-1** changed significantly after being immersed in H_2O_2 for more than 1 day (named **HSTC-1a**). SCXRD analyses revealed that Zn^{2+} coordinates with two imidazolate N atoms of two different purines and two bridging O atoms to form a two-dimensional non-porous framework (Fig. S12†). To ascertain the process of the transformation of **HSTC-1**, we performed *in situ* PXRD experiments by dropping H_2O_2 (or H_2O) on ground **HSTC-1** powder and monitoring results in real-time. The results showed that the PXRD patterns did not change in 48 hours by dropping either H_2O_2 or H_2O (Fig. S2c–f†). We concluded that **HSTC-1** undergoes a crystal transformation in recognition of H_2O_2, which may be attributed to the tautomerism of purine ligands. In solution, the gradual decomposition of H_2O_2 causes electron transfer, and H_2O is a strong ligand, which will cause purine tautomerization and thus change the coordination mode with Zn^{2+} (Fig. S12a†). However, from *in situ* solid-phase PXRD experiments, H_2O_2 guests are protected by the channels of **HSTC-1** from decomposition, resulting in a lack of opportunity for electron transfer, and the structure is unaltered.

To gain further structural information, single-crystal to single-crystal (SC–SC) transformation was performed to *in situ* load H_2O_2 into the framework. Fortunately, the H_2O_2 molecule became locked in the chiral pore of **HSTC-1** and could be verified by SCXRD (denoted as H_2O_2@**HSTC-1**). In addition, H_2O molecules in a 30% H_2O_2 solution are also adsorbed into the pore. The distances between the H of the terminal H_2O_2 and uncoordinated carboxylate O, the H of the terminal H_2O and O of H_2O_2, and the H of the terminal H_2O_2 and the O atom of H_2O are 1.85 Å, 2.34 Å, and 1.84 Å, respectively, which can permit formation of effective hydrogen bonding (Fig. 2d). The formation of H-bond chains between H_2O_2 molecules and between H_2O_2 and H_2O molecules reduces the oxidation effect of H_2O_2 on the host framework. In contrast, the aprotic solvent acetonitrile in pristine **HSTC-1** has no hydrogen bonding interaction over the long distances of the guest and host (4.8–6.3 Å) (Fig. 2c). The above experimental results indicate that the mechanism of **HSTC-1** luminescence quenching in the presence of H_2O_2 may be ascribed to the synergistic effect of the transformation of the framework, competitive absorption and the host–guest and guest–guest interactions.[23]

Inspired by a previously reported purine-based MOF,[21,27] we optimized the synthesis conditions and obtained another Zn(pur)(OAc) MOF, named **HSTC-2**. **HSTC-2** crystallizes in a tetragonal crystal system with a space group of $I\bar{4}$ and possesses a square one-dimensional channel running along the *c*-axis with opening dimensions of *ca.* 7.608 Å × 7.608 Å, while its topology is of the *lig* type (Fig. S8 and ESI† topological analysis). **HSTC-2** has the same asymmetric units and SBUs as **HSTC-1**, with the main difference being the shape and size of the channel. The side views highlighting the channel shape (tube in blue) and pore-metrics analyses[28,29] of **HSTC-1** (Fig. 3a and c) and **HSTC-2** (Fig. 3b and d) allow visualization of the spatial effect. Under the same conditions, the SC–SC transformation of **HSTC-2** loaded with H_2O_2 showed that partially coordinated acetate was oxidized to peroxyacetate, and only H_2O molecules were found in the square channel (Fig. 3e and f). Unfortunately, after soaking for more than 12 h, it was difficult to find good quality crystals for SCXRD data collection, and the frameworks had collapsed using PXRD after filtration. We therefore speculated that the shape and dimensions of the chiral channels play a key role in the recognition of chiral H_2O_2.[6]

We performed metadynamics (MTD) and density functional theory (DFT) calculations to compare the magnitude of energy generated by **HSTC-1**, **HSTC-2** and H_2O_2 during the identification process. One to six H_2O_2 molecules were added into the

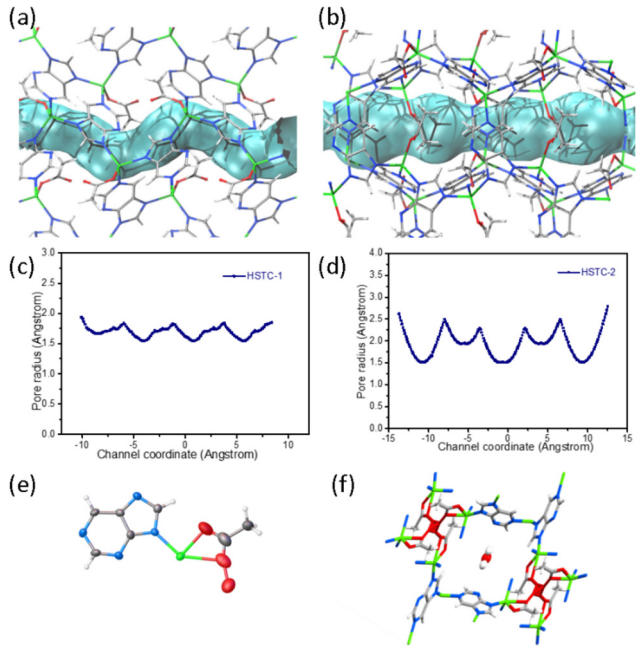

Fig. 3 (a) and (c) Side view of **HSTC-1** highlighting the shape of helical channels (tube in blue) and the pore-metrics analysis (curve in navy), and (b) and (d) the side view of **HSTC-2** highlighting the shape of square channels and the pore-metrics analysis. (e) Asymmetric unit of H_2O_2 oxidized-**HSTC-2**. (f) Crystal structure of oxidized-**HSTC-2** contains only the H_2O guest molecule. Colour codes: C, grey; N, blue; O, red; Zn, green (tetrahedra); H, white.

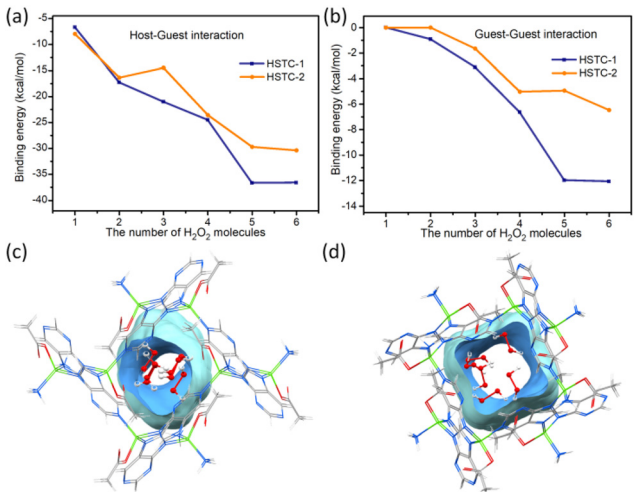

Fig. 4 Binding energies for host–guest interactions (a) and guest–guest interactions (b) in **HSTC-1** and **HSTC-2**; distribution of 6 H_2O_2 molecules in a chiral channel of **HSTC-1** (c) and in a square channel of **HSTC-2** (d).

channel to locate the binding site and find equilibrium structures (see the computation details, Experimental section). The results show that when the first H_2O_2 molecule was added, the average host–guest binding energy of **HSTC-1** was about −6.7 ± 2.05 kcal mol^{-1}, while that of **HSTC-2** was about −7.96 ± 1.15 kcal mol^{-1}. With an increase of the number of H_2O_2 molecules, although an overall slightly larger host–guest binding energy was found in **HSTC-1**, the difference between two isomers was insignificant to distinguish the above experimental results (Fig. 4a and Table S2†). So, the effect of guest–guest interaction is further considered by mapping H_2O_2 molecules in the channel in sequence. As the number of H_2O_2 molecules entering the channel increased, the average guest–guest binding energy of **HSTC-1** was about −12 kcal mol^{-1}, while that of **HSTC-2** was about −5 to −6 kcal mol^{-1}. The difference in the energy of the guest–guest interaction between **HSTC-1** and **HSTC-2** became more significant (Fig. 4b and Table S3†). Meanwhile, the theoretical calculation results indicate that H_2O_2 molecules are distributed more dispersedly in each square channel of **HSTC-2** and tend to only interact with the framework, resulting in weak guest–guest interactions. In this manner, H_2O_2 has a higher chance to oxidize **HSTC-2** to form oxidized-**HSTC-2** or undergo structural transformation. However, on account of the chiral pore of **HSTC-1**, the adsorption of the primary chiral H_2O_2 molecule through the chiral channel induced a series of guests to form a chiral distribution, slowing down the effect of oxidation tendency on the host frameworks. This is consistent with behavior predicted from analysis of the single-crystal structure. The initial incoming H_2O_2 and the host framework exhibit a synergistic effect on the subsequent guest molecules to stack along the chiral rotation axis (Fig. 4c and d).

To demonstrate the encapsulation of H_2O_2 in H_2O_2@**HSTC-1**, the crystals were rinsed with catalase three times (5 ml each) to remove H_2O_2 from the surface, and then treated with 3,3′,5,5′-tetramethyl-benzidine (TMB), a commonly used chromogenic agent for H_2O_2 detection.[30,31] The results showed that **HSTC-1** and H_2O_2@**HSTC-1** barely changed in 30 minutes after the addition of TMB ethanol solution (400 μL, 0.2 M). By adjusting the pH value with buffer, the colour gradually changed from colourless to blue, and an obvious absorption peak appeared at 652 nm, while for **HSTC-1** alone it did not. This is due to the gradual release of H_2O_2 from H_2O_2@**HSTC-1**, oxidizing TMB to ox-TMB after the addition of buffer solution (Fig. 5a). From the time-dependent absorbance plots and the photographs of the TMB chromogenic reaction, it can be seen that oxidized-**HSTC-2** without buffer rapidly changes from colourless to blue, and the absorbance increases continuously until it exceeds the detection range after 1400 s. This is caused by the certain oxidation from the peroxy bond of oxidized-**HSTC-2**. In contrast, the colour of H_2O_2@**HSTC-1** remains unchanged in the absence of buffer solution (Fig. 5b). The above experiments indicate that the chiral channels of **HSTC-1** can temporarily protect H_2O_2, providing a suitable reaction retention time for practical applications.

To quantify the energies of the host–guest interactions between H_2O_2 and **HSTC-1**, isothermal titration calorimetry (ITC) experiments were performed.[32,33] The thermograms obtained by titration of **HSTC-1** suspensions with H_2O_2 showed negative peaks, implying the host–guest interaction

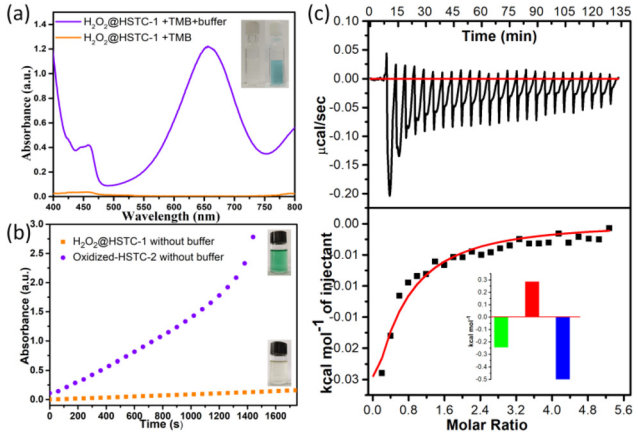

Fig. 5 (a) Comparison of the chromogenic reactions of H_2O_2@**HSTC-1** and **HSTC-1** with TMB. The inset is a photograph of their TMB chromogenic reaction, respectively. (b) The time-dependent absorbance plots of H_2O_2@**HSTC-1** and oxidized-**HSTC-2** after the addition of TMB solution without buffer. The inset is a photographic comparison of their TMB chromogenic reactions. (c) ITC thermogram of the titration of the **HSTC-1** suspension (4 mM, 1.8 mL) with H_2O_2 (99 mM, 15 μL each injection) and fitting with a single-site model. The inset depicts the magnitude of the calculated thermodynamic parameters.

through a favorable exothermic pathway (Fig. 5c). Then, the Gibbs free energy change (ΔG) was calculated to be −528.8 cal mol^{-1}. The $-\Delta G$ and $+\Delta S$ values suggest that the spontaneous processes are mainly due to an enthalpic driving force with a compensating favorable entropic factor. On comparing the effects of H_2O, the ITC experiment involving titration of **HSTC-1** suspensions with H_2O was performed under the same conditions, and no significant thermal changes were observed in the thermogram (Fig. S9†). We speculated that the thermal changes in the system mainly came from the interaction between H_2O_2 and **HSTC-1** frameworks.

Conclusions

In summary, utilizing purine biomolecules as ligands, we successfully synthesized fluorescent **HSTC-1** with chiral pores, which spontaneously identify and capture H_2O_2. The H_2O_2 and H_2O guests stack along the chiral rotation axis in chiral helical channels due to a synergistic effect between initial incoming H_2O_2 and the host framework, decreasing the oxidation of the framework. The resulting unique MOF, **HSTC-1**, can successfully use the chiral channel to slow down the attack of the strong oxidizing agent H_2O_2, thus exhibiting higher reaction retention, which provides a new perspective for the construction of intelligent protective matrix materials, and has potential applications in biopharmacology and cutting-edge medicine. Although there is still a long way to go until reliable optical H_2O_2 sensors can be used for quantitative and continuous measurements, we propose that in the future, bioinspired luminescent MOFs will become feasible platforms for simple, rapid and accurate determination of H_2O_2 concentrations in biological systems.

Experimental

Materials and methods

All chemicals were purchased from commercial sources and used without further purification. The organic solutions were purchased from Xilong Science Co., Ltd and Guangdong Guanghua Technology Co., Ltd. Single-crystal X-ray diffraction (SCXRD) analysis was performed using a Rigaku XtaLAB PRO MM007-DW diffractometer system, an RA-Micro7HF-MR-DW (Cu/Mo) X-ray generator and a Pilatus 3R-200K-A detector (Cu Kα, λ = 1.54178 Å). PXRD patterns of the bulk samples were measured on a Rigaku MiniFlex600 X-ray diffractometer (Rigaku, Kyoto, Japan). ITC experiments were conducted on a Malvern MicroCal VP-ITC System (Malvern, Europe). Elemental analyses of C, H, and N were carried out on a PerkinElmer PE 2400II. pH was confirmed using a PHS-3C pH meter. Thermogravimetric analyses (TGA) were performed using a Shimadzu synchronous differential thermal-thermogravimetric analyzer (DTG-60) in the temperature range of room temperature to 800 °C under nitrogen flow (40 mL min^{-1}) at a typical heating rate of 10 °C min^{-1}. Infrared spectra (IR) were collected in KBr disks using a Shimadzu IRAffinity-1 in the range of 4000–400 cm^{-1}. Solid-state and solution luminescence spectra were measured on a PF-5301PC. UV-Vis spectra and results of ultraviolet titrating experiments were recorded on a TU-1950 ultraviolet and visible spectrophotometer (Persee, Beijing, China). Circular dichroism (CD) spectra were recorded on a Chirascan V100 (Applied Photophysics Ltd, UK) in the range of 200–500 nm (equipped with a PMT detector).

Synthesis of HSTC-1. A mixture of $Zn(CH_3COO)_2{\cdot}2H_2O$ (0.12 mmol), purine (0.04 mmol), and acetonitrile (5 mL) was sealed in a Pyrex glass tube with the pH adjusted using 50 μL of 28% NH_3 aqueous solution, and heated in an oven at 120 °C for 72 h. After cooling to room temperature at a rate of 5 °C h^{-1}, colourless crystals were obtained by filtration and washed with acetonitrile 3 times. Selected suitable crystals were immediately mounted on the single-crystal X-ray diffractometer for structural determination. IR spectrum (see Fig. S4a†): 3427(s), 3103(w), 1907(w), 1617(s), 1418(s), 1407(s), 1319(s), 1211(s), 1099(m), 1018(m), 958(s), 800(s), 646(s). Elemental analysis (CHN), $C_7H_6N_4O_2Zn(H_2O)_{1.2}$, calculated (%): C, 31.7076; H, 3.1931; N, 21.1298. Found (%): C, 31.19; H, 3.116; N, 21.47.

Synthesis of HSTC-2. A mixture of $Zn(CH_3COO)_2{\cdot}2H_2O$ (0.12 mmol), purine (0.04 mmol), and acetonitrile (5 ml) was sealed in a Pyrex glass tube with the pH adjusted using 400 μL of 1 M HNO_3, and heated in an oven at 120 °C for 72 h. After cooling to room temperature at a rate of 5 °C h^{-1}, yellowish crystals were obtained by filtration and washing with acetonitrile 3 times. Selected suitable crystals were immediately mounted on the single-crystal X-ray diffractometer for structural determination. IR spectrum (see Fig. S4b†). 3416(s),

3114(w), 1907(w), 1619(s), 1480(m), 1408(s), 1314(s), 1209(s), 1096(m), 953(s), 799(s), 657(s).

Fluorescence titration experiments

10 mg of the **HSTC-1** solid sample was fully ground into powders and then transferred to a 10 mL volumetric flask. Acetonitrile was added and sonicated for 30 min to form a uniformly dispersed MOF suspension (1 mg mL^{-1}). The suspension was further diluted to the corresponding concentrations with acetonitrile for concentration-dependent fluorescence titration experiments. To 2.50 mL of the above suspensions, 10 μL of H_2O_2 solution (1 M, 0.1 M, 0.01 M, 1 mM, 0.1 mM) was incrementally added to monitor the fluorescence emission intensity (λ_{max} = 380 nm) until the endpoint.

TMB oxidation experiments

In a typical assay, 200 μL of TMB ethanol solution (0.2 M, 0.1 M), 1.5 mL of ethanol, 1.5 mL of 1 mg mL^{-1} **HSTC-1** (or H_2O_2@**HSTC-1**) suspension, and 200 μL of H_2O, were sequentially placed into a 5 mL vial with (or without) sodium acetate buffer solution (pH 5.0). The mixture (with a total volume of 3.4 mL) was stirred and then filtered through a syringe filter (PTFE, hydrophobic, 0.24 μm). The content of oxTMB in the filtrate was assessed through UV-Vis absorbance.

The steady-state kinetic assays were performed through the oxidation of TMB in the presence of H_2O_2 to produce blue products. The substrate solution was prepared by dissolving TMB in 2 mL of 30% ethanol solution. The formation of oxTMB was determined by UV-Vis spectrophotometry at 652 nm after adding 1 mg of MOFs (H_2O_2@**HSTC-1** or oxidized-**HSTC-2**) to the substrate solution.

Isothermal titration calorimetry (ITC) experiments

In a typical titration, H_2O_2 solution was incrementally added to the ITC sample cell containing an aqueous suspension of **HSTC-1**. All titration experiments were performed in aqueous solution without adjusting pH under the following conditions: reference power (10–15 μcal s^{-1}), initial injection delay (300 s), stirring speed (850 rpm), feedback mode gain (high feedback), the spacing between injections (300 s), and filter period (10 s). The thermodynamic profile of each binding process was calculated by fitting the data with a single site interaction model.

Computation details

The computational models are extracted from the single-crystal structures of **HSTC-1** and **HSTC-2**, containing sixteen Zn^{2+} cations, sixteen adenine ligands, and sixteen acetate anions. All Zn^{2+} cations are retained in a tetrahedral four-coordination mode by completing coordinated N atoms as NH_3; hydrogen atoms are added to adenine ligands to maintain the neutral framework. All hydrogen atoms are optimized with Gaussian 16 at the BLYP level of theory and 6-31G* basis sets.[34–37] To study the host–guest and/or guest–guest interactions, one to six hydrogen peroxide molecules are added into the channel to locate the binding site and find equilibrium structures by adopting Crest 2.11.2 software and GFN-FF force field.[38,39] Metadynamics (MTD) algorithms are used to acquire all possible structures at 298.15 K within a 5 kcal mol^{-1} window from the lowest-energy structure.[40] The five lowest energy structures of $(H_2O_2)_{1-6}$@**HSTC-1/2** are screened to be optimized by GFN2-xTB methods in order to obtain the defined binding sites with xtb 6.4.0 software, in which an ALPB water solvation model is implicitly used.[41,42] Binding energies are calculated with the ORCA 4.2.1 software package at the BLYP level of theory.[43,44] Def2-SVP basis sets, along with auxiliary Def2/J and Def2-SVP/C, are adopted for Zn, O, N, C, and H atoms.[45,46] Solvation is treated by the SMD water solvation model.[47] Grimme's D4 method and geometrical counterpoise (gCP) are considered for dispersion interaction corrections and to overcome the basis set superposition error (BSSE) when using small basis sets, respectively.[48,49]

Author contributions

H. Cai conceived and wrote the manuscript and supervised the research; D. Li supervised the research and polished the manuscript; J.-W. Wu, X.-J. Cai, Y.-Y. Huang, Y.-H. Lu, J.-W. Cai, and W. Lu conducted the synthesis and fluorescence, UV-Vis, CD and TMB testing experiments; J.-X. Sun and Z.-L. Yuan contributed to SCXRD and PXRD data experiments and analysis; H.-Y. Zhang conducted TG and IR experiments; Y.-L. Lai conducted ITC experiments and analysis. Z. Lu conducted the theoretical calculations. All authors read and commented on the manuscript.

Conflicts of interest

There are no conflicts to declare.

Acknowledgements

This work was financially supported by the National Natural Science Foundation of China (No. 21731002, 21975104, 22150004 and 21701038), the Guangdong Major Project of Basic and Applied Research (2019B030302009), the Guangdong Basic and Applied Basic Research Foundation (2023A1515010868), the Special Projects in Key Fields from the Department of Education of Guangdong Province (2021ZDZX2065), the Guangdong Provincial Key Laboratory of Functional Substances in Medicinal Edible Resources and Healthcare Products (2021B1212040015), the Open Fund of Guangdong Provincial Key Laboratory of Functional Supramolecular Coordination Materials and Applications (2020B121201005), and the Scientific Research Funds of Hanshan Normal University (QD202201, PNB2101). We are indebted to the X-ray single crystal diffraction laboratory of Hanshan Normal University for support. We are also grateful to Guang-Wei Wu for his help in crystal analysis.

References

1 E. A. Veal, A. M. Day and B. A. Morgan, Hydrogen Peroxide Sensing and Signaling, *Mol. Cell*, 2007, **26**, 1–14.

2 M. Moßhammer, M. Kühl and K. Koren, Possibilities and Challenges for Quantitative Optical Sensing of Hydrogen Peroxide, *Chemosensors*, 2017, **5**, 28.

3 D. Gough and T. Cotter, Hydrogen peroxide: a Jekyll and Hyde signalling molecule, *Cell Death Dis.*, 2011, **2**, e213.

4 F. Antunesa and P. M. Brito, Quantitative biology of hydrogen peroxide signaling, *Redox Biol.*, 2017, **13**, 1–7.

5 J. Meier, E. M. Hofferber, J. A. Stapleton and N. M. Iverson, Hydrogen Peroxide Sensors for Biomedical Applications, *Chemosensors*, 2019, **7**, 64.

6 J. Zhou, J. Duan, X.-E. Zhang, Q. Wang and D. Men, A chiral responsive carbon dots-gold nanoparticle complex mediated by hydrogen peroxide independent of surface modification with chiral ligands, *Nanoscale*, 2018, **10**, 18606; C. Liu and Y. Yin, The Most Simple Chiral Molecules–H_2O_2 and H_2S, *J. Beijing Inst. Petro-chem. Technol.*, 1998, **6**, 22.

7 Y. Cui, F. Chen and X.-B. Yin, A ratiometric fluorescence platform based on boric-acid-functional Eu-MOF for sensitive detection of H_2O_2 and glucose, *Biosens. Bioelectron.*, 2019, **135**, 208.

8 F. Luo, Y. Lin, L. Zheng, X. Lin and Y. Chi, Encapsulation of Hemin in Metal−Organic Frameworks for Catalyzing the Chemiluminescence Reaction of the H_2O_2−Luminol System and Detecting Glucose in the Neutral Condition, *ACS Appl. Mater. Interfaces*, 2015, **7**, 11322.

9 S. Banerjee, C. T. Lollar, Z. Xiao, Y. Fang and H.-C. Zhou, Biomedical Integration of Metal–Organic Frameworks, *Trends Chem.*, 2020, **2**, 467.

10 H. Lyu, O. I. Chen, N. Hanikel, M. I. Hossain, R. W. Flaig, X. Pei, A. Amin, M. D. Doherty, R. K. Impastato, T. G. Glover, D. R. Moore and O. M. Yaghi, Carbon Dioxide Capture Chemistry of Amino Acid Functionalized Metal–Organic Frameworks in Humid Flue Gas, *J. Am. Chem. Soc.*, 2022, **144**, 2387.

11 T. Wang, W. Mei, P. Li, Y.-L. Peng, Y. Chen, J.-G. Ma, P. Cheng, M. Fang, K. Yu and Z. Zhang, Boosting C_2H_2/CO_2 separation of metal–organic frameworks via anion exchange and temperature elevation, *J. Mater. Chem. A*, 2022, **10**, 22175.

12 L. Liu, Y. Li, L. Wang and Z. Xie, Modulating charge transfer over metal–organic framework nanocomposites for NIR light-boosted photothermal conversion, *J. Mater. Chem. A*, 2022, **10**, 20794.

13 J. An, S. J. Geib and N. L. Rosi, Cation-Triggered Drug Release from a Porous Zinc−Adeninate Metal−Organic Framework, *J. Am. Chem. Soc.*, 2009, **131**, 8376.

14 J. An, S. J. Geib and N. L. Rosi, High and selective CO_2 uptake in a cobalt adeninate metal-organic framework exhibiting pyrimidine- and amino-decorated pores, *J. Am. Chem. Soc.*, 2010, **132**, 38.

15 I. Imaz, M. Rubio-Martínez, J. An, I. Solé-Font, N. L. Rosi and D. Maspoch, Metal–biomolecule frameworks (MBioFs), *Chem. Commun.*, 2011, **47**, 7287.

16 S. Tashiro, K. Nakata, R. Hayashi and M. Shionoya, Multipoint Hydrogen Bonding-Based Molecular Recognition of Amino Acids and Peptide Derivatives in a Porous Metal-Macrocycle Framework: Residue-Specificity, Diastereoselectivity, and Conformational Control, *Small*, 2021, **17**, 2005803.

17 H. Cai, Y.-L. Huang and D. Li, Biological metal–organic frameworks: Structures, host–guest chemistry and bio-applications, *Coord. Chem. Rev.*, 2019, **378**, 207.

18 H. Cai, M. Li, X.-R. Lin, W. Chen, G.-H. Chen, X.-C. Huang and D. Li, Spatial, hysteretic, and adaptive host-guest chemistry in a metal–organic framework with open Watson-crick sites, *Angew. Chem., Int. Ed.*, 2015, **54**, 10454.

19 S. L. Anderson, P. G. Boyd, A. Gładysiak, T. N. Nguyen, R. G. Palgrave, D. Kubicki, L. Emsley, D. Bradshaw, M. J. Rosseinsky, B. Smit and K. C. Stylianou, Nucleobase Pairing and Photodimerization in a Biologically Derived Metal-Organic Framework Nanoreactor, *Nat. Commun.*, 2019, **10**, 1612.

20 S. Chand, O. Alahmed, W. S. Baslyman, A. Dey, S. Qutub, R. Saha, Y. Hijikata, M. Alaamery and N. M. Khashab, DNA-Mimicking Metal–Organic Frameworks with Accessible Adenine Faces for Complementary Base Pairing, *JACS Au*, 2022, **2**(3), 623.

21 R. Lyndon, Y. Wang, I. M. Walton, Y. Ma, Y. Liu, Z. Yu, G. Zhu, S. Berens, Y.-S. Chen, S. G. Wang, S. Vasenkov, D. S. Sholl, K. S. Walton, S. H. Pang and R. P. Lively, Unblocking a rigid purine MOF for kinetic separation of xylenes, *Chem. Commun.*, 2022, **58**, 12305.

22 H. Cai, Y.-X. Wu, Z. Lu, D. Luo, J.-X. Sun, G.-W. Wu, M. Li, Y.-B. Wei, L.-M. Zhong and D. Li, Mimicking DNA Periodic Docking Grooves for Adaptive Identification of $_L$-/$_D$-tryptophan in a Biological Metal-Organic Framework, *J. Am. Chem. Soc.*, 2022, **144**, 9559.

23 Y.-L. Huang, P.-L. Qiu, J.-P. Bai, D. Luo, W. Lu and D. Li, Exclusive Recognition of Acetone in a Luminescent BioMOF through Multiple Hydrogen-Bonding Interactions, *Inorg. Chem.*, 2019, **58**, 7667.

24 B. Pullman and A. Pullman, Electronic Aspects of Purine Tautomerism, *Adv. Heterocycl. Chem.*, 1971, **13**, 77.

25 E. D. Raczyńska, J.-F. Gal, P.-C. Maria, B. Kamińska, M. Igielska, J. Kurpiewski and W. Juras, Purine tautomeric preferences and bond-length alternation in relation with protonation-deprotonation and alkali metal cationization, *J. Mol. Model.*, 2020, **26**, 93.

26 S. A. Diamantis, A. Margariti, A. D. Pournara, G. S. Papaefstathiou, M. J. Manos and T. Lazarides, Luminescent metal-organic frameworks as chemical sensors: common pitfalls and proposed best practices, *Inorg. Chem. Front.*, 2018, **5**, 1493.

27 J. Kahr, J. P. S. Mowat, A. M. Z. Slawin, R. E. Morris, D. FairenJimenez and P. A. Wright, Synthetic control of framework zinc purinate crystallisation and properties of a

large pore, decorated, mixed-linker RHO-type ZIF, *Chem. Commun.*, 2012, **48**, 6690.
28 O. S. Smart, J. M. Goodfellow and B. A. Wallace, The Pore Dimensions of Gramicidin A, *Biophys. J.*, 1993, **65**, 2455.
29 W. Humphrey, A. Dalke and K. Schulten, HOLE: A program for the analysis of the pore dimensions of ion channel structural models, *J. Mol. Graphics*, 1996, **14**, 33.
30 Y. Yang, Y. Gong, X. Li, M. Li, Q. Wei, B. Zhou and J. Zhang, Alkaline-Stable Peroxidase Mimics Based on Biological Metal–Organic Frameworks for Recyclable Scavenging of Hydrogen Peroxide and Detecting Glucose in Apple Fruits, *ACS Sustainable Chem. Eng.*, 2022, **10**(32), 10685.
31 H.-Q. Zheng, C. Lin, R. Cao, Z.-J. Lin and J.-W. Su, MOF-808: A Metal–Organic Framework with Intrinsic PeroxidaseLike Catalytic Activity at Neutral pH for Colorimetric Biosensing, *Inorg. Chem.*, 2018, **57**(15), 9096.
32 Y.-B. Wei, D. Luo, X. Xiong, Y.-L. Huang, M. Xie, W. Lu and D. Li, Biomimetic Mimicry of Formaldehyde-Induced DNA–Protein Crosslinks in the Confined Space of Metal–Organic Framework, *Chem. Sci.*, 2022, **13**, 4813; Y.-B. Wei, M.-J. Wang, D. Luo, Y.-L. Huang, M. Xie, W. Lu, X. Shu and D. Li, Ultrasensitive and highly selective detection of formaldehyde via an adenine-based biological metal organic framework, *Mater. Chem. Front.*, 2021, **5**, 2416.
33 R. J. Drout, S. Kato, H. Chen, F. A. Son, K. Otake, T. Islamoglu, R. Q. Snurr and O. K. Farha, Isothermal Titration Calorimetry to Explore the Parameter Space of Organophosphorus Agrochemical Adsorption in MOFs, *J. Am. Chem. Soc.*, 2020, **142**, 12357.
34 M. J. Frisch, G. W. Trucks, H. B. Schlegel, G. E. Scuseria, M. A. Robb, J. R. Cheeseman, G. Scalmani, V. Barone, G. A. Petersson, H. Nakatsuji, X. Li, M. Caricato, A. V. Marenich, J. Bloino, B. G. Janesko, R. Gomperts, B. Mennucci, H. P. Hratchian, J. V. Ortiz, A. F. Izmaylov, J. L. Sonnenberg, D. Williams-Young, F. Ding, F. Lipparini, F. Egidi, J. Goings, B. Peng, A. Petrone, T. Henderson, D. Ranasinghe, V. G. Zakrzewski, J. Gao, N. Rega, G. Zheng, W. Liang, M. Hada, M. Ehara, K. Toyato, R. Fukuda, J. Hasegawa, M. Ishida, T. Nakajima, Y. Honda, O. Kitao, H. Nakai, T. Vreven, K. Throssell, J. A. Montgomery Jr., J. E. Peralta, F. Ogliaro, M. J. Bearpark, J. J. Heyd, E. N. Brothers, K. N. Kudin, V. N. Staroverov, T. A. Keith, R. Kobayashi, J. Normand, K. Raghavachari, A. P. Rendell, J. C. Burant, S. S. Iyengar, J. Tomasi, M. Cossi, J. M. Millam, M. Klene, C. Adamo, R. Cammi, J. W. Ochterski, R. L. Martin, K. Morokuma, O. Farkas, J. B. Foresman and D. J. Fox, *Gaussian 16*, Gaussian Inc., 2016.
35 A. D. Becke, Density-Functional Exchange-Energy Approximation with Correct Asymptotic Behavior, *Phys. Rev. A*, 1988, **38**, 3098.
36 C. Lee, W. Yang and R. G. Parr, Development of the Colle-Salvetti Correlation-Energy Formula into a Functional of the Electron Density, *Phys. Rev. B: Condens. Matter Mater. Phys.*, 1988, **37**, 78.
37 G. A. Petersson, A. Bennett, T. G. Tensfeldt, M. A. A. Laham, W. A. Shirley and J. Mantzaris, A Complete Basis Set Model Chemistry. I. The Total Energies of Closed–shell Atoms and Hydrides of the First–row Elements, *J. Chem. Phys.*, 1988, **89**, 2193.
38 P. Pracht, F. Bohle and S. Grimme, Automated Exploration of the Low-Energy Chemical Space with Fast Quantum Chemical Methods, *Phys. Chem. Chem. Phys.*, 2020, **22**, 7169.
39 S. Spicher and S. Grimme, Robust Atomistic Modeling of Materials, Organometallic, and Biochemical Systems, *Angew. Chem., Int. Ed.*, 2020, **59**, 15665.
40 S. Grimme, Exploration of Chemical Compound, Conformer, and Reaction Space with Meta-Dynamics Simulations Based on Tight-Binding Quantum Chemical Calculations, *J. Chem. Theory. Comput.*, 2019, **15**, 2847.
41 C. Bannwarth, E. Caldeweyher, S. Ehlert, A. Hansen, P. Pracht, J. Seibert, S. Spicher and S. Grimme, Extended Tight–binding Quantum Chemistry Methods, *Wiley Interdiscip. Rev.: Comput. Mol. Sci.*, 2021, **11**, e1493.
42 S. Bannwarth, S. Ehlert and S. Grimme, GFN2-xTB—An Accurate and Broadly Parametrized Self-Consistent Tight-Binding Quantum Chemical Method with Multipole Electrostatics and Density-Dependent Dispersion Contributions, *J. Chem. Theory Comput.*, 2019, **15**, 1652.
43 F. Neese, The ORCA Program System, *Wiley Interdiscip. Rev.: Comput. Mol. Sci.*, 2011, **2**, 73.
44 F. Neese, Software Update: The ORCA Program System, Version 4.0, *Wiley Interdiscip. Rev.: Comput. Mol. Sci.*, 2017, **8**, e1327.
45 F. Weigend and R. Ahlrichs, Balanced Basis Sets of Split Valence, Triple Zeta Valence and Quadruple Zeta Valence Quality for H to Rn: Design and Assessment of Accuracy, *Phys. Chem. Chem. Phys.*, 2005, **7**, 3297–3305.
46 F. Weigend, Accurate Coulomb-Fitting Basis Sets for H to Rn, *Phys. Chem. Chem. Phys.*, 2006, **8**, 1057.
47 A. V. Marenich, C. J. Cramer and D. G. Truhlar, Universal Solvation Model Based on Solute Electron Density and on a Continuum Model of the Solvent Defined by the Bulk Dielectric Constant and Atomic Surface Tensions, *J. Phys. Chem. B*, 2009, **113**, 6378.
48 E. Caldeweyher, S. Ehlert, A. Hansen, H. Neugebauer, S. Spicher, C. Bannwarth and S. Grimme, A Generally Applicable Atomic-Charge Dependent London Dispersion Correction, *J. Chem. Phys.*, 2019, **150**, 154122.
49 H. Kruse and S. Grimme, A Geometrical Correction for the Inter- and Intra-Molecular Basis Set Superposition Error in Hartree-Fock and Density Functional Theory Calculations for Large Systems, *J. Chem. Phys.*, 2012, **136**, 154101.